

# A Highly Robust Contact Sensor for Precise Contact Detection of Fabric

Zhengrong Ling<sup>1\*</sup>, Lanxuan Hong<sup>1\*</sup>, Xiong Yang<sup>1</sup>, Yifeng Tang<sup>2</sup>, Dong Guo<sup>2</sup> and Yajing Shen<sup>3</sup>

**Abstract**— Automation in the apparel and textile industry has long been a pursuit. However, accurately locating the surface of a fabric remains a challenge, limiting the automation in sorting, packaging, and other processes. When humans locate clothing, they rely on contact feedback for the exact position of the clothing surface. As existing contact detection solutions are significantly affected by environmental factors, it is essential to develop a sensor with robust contact detection capabilities. In this work, we introduce a contact sensor with high robustness and high force resolution. This contact sensor detects contact by measuring the deformation of an elastomer using a distance-measuring module. Based on the deformation characteristics of the elastomer, we designed a detection algorithm that not only reduces the noise of data but also extracts features such as trends and elastomer states, enabling reliable contact detection. Through experiments, we validated that this contact sensor can detect contact forces as low as 0.017 N and is robust to external interference or sensor movement. We also verified that the sensor can process data within 7.5 ms and return contact detection with 95% accuracy. Additionally, we assessed its effectiveness in real fabric contact scenarios.

## I. INTRODUCTION

The automation of the apparel and textile industry is a long-standing pursuit to enhance efficiency and reduce costs. Over the years, automation has been implemented in most processes, including cutting [1], sewing [2], and ironing [3] of clothing. However, accurately determining the surface position of the clothing still poses significant challenges.

Although non-contact measurement devices, such as laser rangefinders and cameras have been successfully applied in surface reconstruction and localization [4], [5], they still have limitations by resolution and are affected by lighting conditions and surface reflectivity. In contrast, humans perceive their environment through active contact [6], [7], which enables them to acquire reliable positional information. This method of localization through contact has inspired the positioning of fabric surfaces on robots.

Traditional sensors for contact detection include various force sensors, such as capacitive and piezoelectric sensors

[8], [9], [10], which offer precise contact detection capabilities. However, these sensors are susceptible to temperature and humidity [11], resulting in the accuracies often failing for application. Through precise packaging and anti-interference design, scientists have developed robust, high-precision FT (Force-Torque) sensors. These sensors, typically designed for robotic wrists, enable accurate contact detection for tasks such as robotic assembly[12], [13]. However, the sensitivity of FT sensors to small forces comes at the cost of their inherent fragility, making them prone to damage [14]. Furthermore, since the gripper is not entirely rigid, small contact forces may be absorbed by the gripper mechanism, thereby reducing the force resolution of the FT sensor.

The advent of fingertip tactile sensors has ushered in a realm of new possibilities. Vision-based tactile sensors analyze contact forces by detecting elastomer deformation caused by contact through a camera [15], [16] providing excellent texture information of the contacted object. However, this approach requires a computationally intensive model to analyze images to determine the contact states [17]. Alternatively, magnetic-based tactile sensors can provide force feedback through self-decoupling properties, eliminating the need for complex calculations [18]. However, external magnetic objects in the environment can cause these sensors to fail [19]. Pressure-based tactile sensors detect contact by measuring air pressure changes, generating signals in response to contact forces achieving high contact localization accuracy [20]. However, these sensors are sensitive to temperature and need frequent calibration. The optoelectronic-based sensors detect the deformation of elastomers by the phototransistor inside, providing a convenient and stable contact force detecting method [21]. However, the structure and algorithms, however, are still at a preliminary stage, restricting the force resolution and thus limiting their potential applications.

In the field of fabric surface positioning, traditional sensors are still in their infancy. Challenges such as poor robustness, limited resolution, and high computational load, hinder their adoption in practical applications. To address these issues, we propose a novel contact sensor based on structure and algorithm design, exhibiting the following characteristics:

- 1) High Force Resolution: Capable of detecting a minimum contact force of 0.017 N, suitable for soft materials such as down jackets and wool;
- 2) Strong Robustness: Unaffected by external interference such as temperature, lighting magnetic fields, and high-speed motion;
- 3) Low Computational Load: Able to complete detection algorithm within 7.5 ms on CPU(2.20GHz);
- 4) High Detection Accuracy: Achieve 95% accuracy.

\*These authors contributed equally to this work

<sup>1</sup>Zhengrong Ling, Lanxuan Hong, Xiong Yang are with the Department of Electronic and Computer Engineering, the Hong Kong University of Science and Technology, Kowloon, Hong Kong, zlingab@connect.ust.hk, lhongae@connect.ust.hk, eexiongyang@ust.hk

<sup>2</sup>Yifeng Tang, Dong Guo are with the Department of Biomedical Engineering, City University of Hong Kong, Hong Kong yf.tang@my.cityu.edu.hk, dongguo3-c@my.cityu.edu.hk

<sup>3</sup>Yajing Shen is with the Department of Electronic and Computer Engineering & Research Center on Smart Manufacturing, the Hong Kong University of Science and Technology, Kowloon, Hong Kong eeyajing@ust.hk

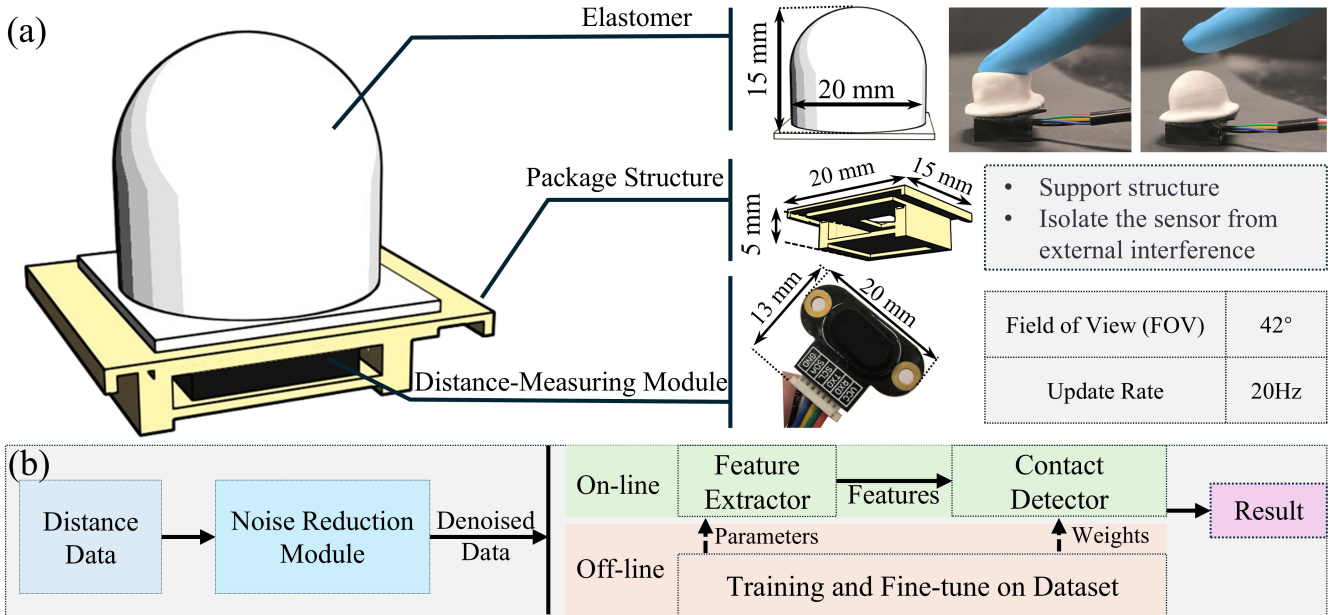


Fig. 1. Overview of the contact sensor. (a) illustrates the hardware components of the contact sensor. (b) presents the structure of the contact detection algorithm used by the contact sensor.

## II. DESIGN & FABRICATION

### A. Principles of the Contact Sensor

The proposed contact sensor consists of three components, as shown in Fig. 1(a), including an elastomer, a packaging structure, and a distance-measuring module.

The elastomer is hollow, shaped as a combination of a cylinder and a hemisphere, deforms upon contact with external objects and returns to its original shape afterward. The packaging structure supports the entire contact sensor, fixing the elastomer at its edges. Inside the package, a distance-measuring module is installed beneath the elastomer. It is an off-the-shelf ToF (Time-of-Flight) module, which can measure the distance of the object within the FOV (Field of View). In our study, the FOV is 42° directed towards the cavity of the elastomer. With a frequency of 20 Hz, the distance-measuring module outputs a single value in each measuring period. The output value represents the smallest distance in the FOV, which varies during contact detection.

The data collected by the distance-measuring module goes through a pipeline for processing and decision, as shown in Fig. 1(b). The first stage is data collection, followed by the Noise Reduction Module to filter the raw collected data in real-time. After this, a feature extraction module is applied to the denoised data. This module extracts features that effectively characterize the contact state, including cluster, trend and magnitudes, and thereby improving the accuracy and robustness of the detection. Finally, these features are forwarded to the detector to ascertain the contact status. This entire process is efficient in terms of computational resources and supports real-time online execution.

### B. Fabrication of Elastomer and Contact Analysis

The elastomer, composed of silica gel, is fabricated using a casting method as shown in Fig. 2. A 3D-printed mold consisting of a convex and a concave component is prepared. The convex mold, shaped as a cylinder and hemisphere, pairs with a concave mold to create a 0.4 mm gap. Liquid silica gel mixed with reflective powder is injected into this cavity as shown in Fig. 2(b) and cured at 75°C for 45 minutes, resulting in a soft elastomer.

The elastomer is then affixed on the packaging structure, covering both the emitter and collector as shown in Fig. 3. The collector captures reflected laser signals within a 42° field of view. By measuring the time interval between laser emission and the earliest reflected signal, the distance to an object is calculated considering the speed of light.

As shown in Fig. 3, due to the hemispherical shape, some lasers return faster than others. The module prioritizes the fastest returning signal, establishing an effective measurement plane. As contact force increases, the elastomer deforms, altering the effective measurement plane. This process has three stages as shown in Fig. 3. Initially, with no contact, the elastomer is in its original state, yielding a normal measurement value. When contact occurs with low force, minimal deformation leads to a rise in uncontacted areas, increasing the effective measurement distance. As the deformation continues to increase, the laser returning from the contact point reaches the receiving end more quickly, resulting in a decrease in effective measurement distance.

When the sensor contacts the fabric, it experiences a contact force  $F_s$  from the fabric and exerts an equal force  $F_m = F_s$  on it. This force causes deformation in the fabric, denoted as  $\Delta h$ . As shown in Fig. 4(a), when deformation is small, the fabric is in a structural fluffy state. In this

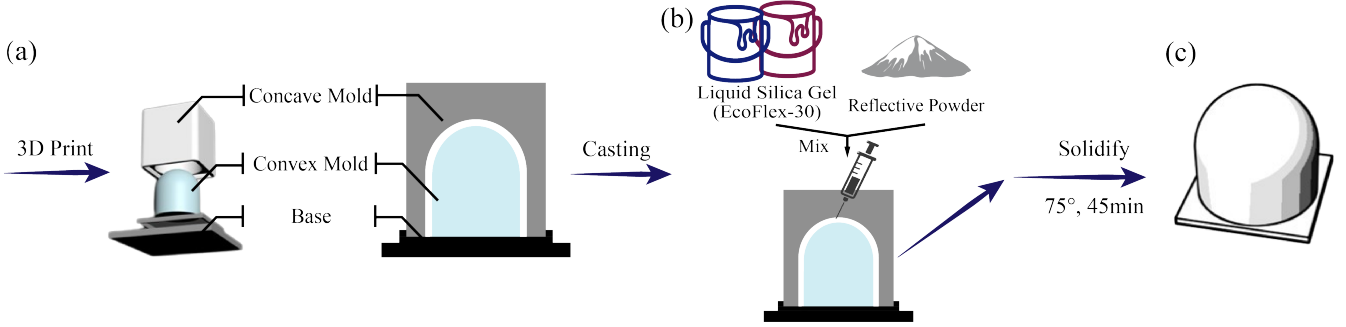


Fig. 2. Fabrication of the elastomer. (a) shows the mold used for fabricating the elastomer. (b) illustrates the casting of the elastomer, where a mixture of liquid silicone and reflective powder is poured into the gaps between the convex and concave molds. (c) presents the elastomer after curing and demolding.

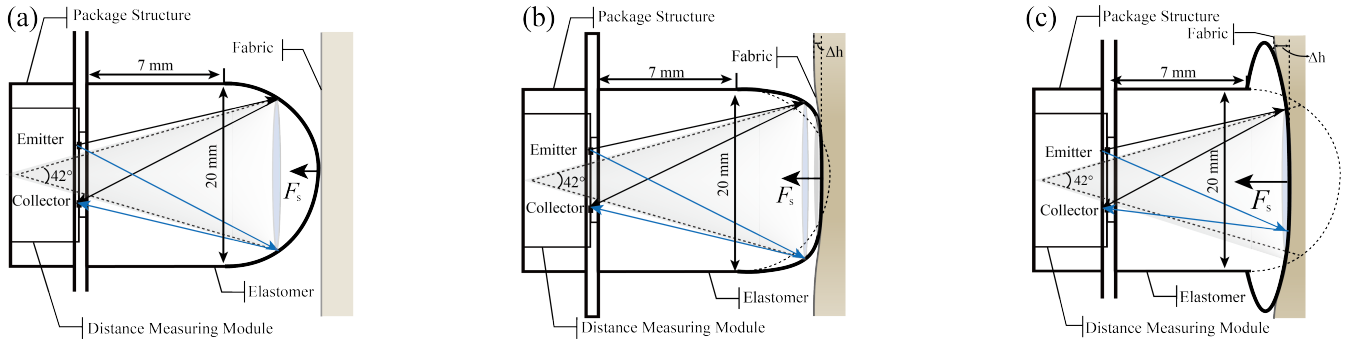


Fig. 3. Deformation states of the elastomer under different contact forces. The FOV of the distance-measuring module is indicated by gray shading. The ellipses within the elastomer represent equidistant planes where the reflected laser travels equal path lengths. The brown object outside the elastomer represents the fabric. (a) Deformation state under no contact. (b) Deformation state under light contact. (c) Deformation state under forceful contact.

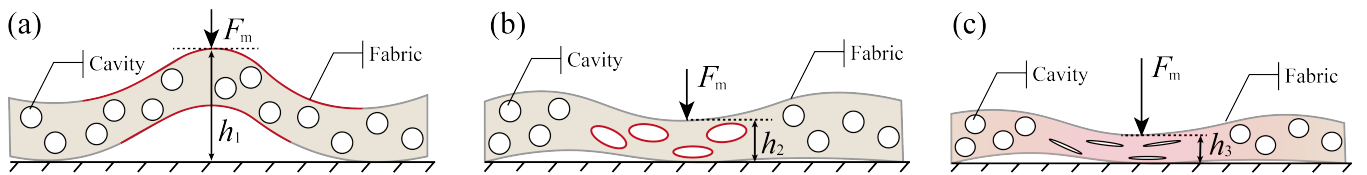


Fig. 4. Three states related to fabric deformation. (a) Shows the structural fluffy state, where the fabric supports a hollow structure. (b) indicates the material fluffy state, where the shape of the fabric is primarily determined by the internal cavities. (c) illustrates the unfluffy state, where the fabric has been compressed to a nearly solid state.

case, the distance  $h_1$  between fabric surfaces depends on the fabric thickness, cavity size, and hollow structure, with  $\Delta h$  primarily affected by the deformation of the fluffy structure.

As the contact force  $F_m$  increases, the fluffy structure diminishes, shifting the dominant factor affecting  $\Delta h$  to the size of the internal cavities, placing the fabric in a material fluffy state as shown in Fig. 4(b). If the contact force continues to rise, the internal cavities will vanish, and the inherent elasticity of the material will dominate  $\Delta h$ , resulting in an unfluffy state as shown in Fig. 4(c). Since the unfluffy fabric is considered as being integrated with the next layer for robot gripper, effective contact detection occurs only when the contacts in either the structural or material fluffy state.

### C. Design of the Contact Detection Algorithm

A pipeline, as shown in Algorithm 1, is developed, generating a contact detection for each detected distance data  $d$ . A steady stream of detected distance data, processed one at a time, will pass through all three parts of the pipeline,

including noise reduction, feature extraction, and contact decision. For each detected distance, a contact state  $s_t$  is generated indicating whether a contact has occurred.

*1) Noise Reduction:* The noise reduction step is designed to reduce noise in the raw distance measurements. A filter along with a smoothing operation is deployed to denoise both the detected distance data, integrating current measurements with the local historical context. We applied the Kalman filter on each obtained distance data  $d$  to get  $d_f$ . A smoothing method is implemented on  $d_f$  to reduce local fluctuations of detected distance data, allowing for features to be extracted closer to the actual conditions. The smoothing is performed as follows:

$$\hat{d}_i = d_{f,i} \cdot \alpha + \hat{d}_{i-1} \cdot (1 - \alpha)$$

where the smoothing factor  $\alpha$  is adjusted to 0.8, which is a trade-off between the immediacy of the filtered data and robustness to outliers. Specifically, a higher value of  $\alpha$  would improve the immediacy but reduce the robustness to outliers.

---

**Algorithm 1** Contact Detection

- 1: **Input:** Distance  $\hat{d}_{t-w:t}$ , Logistic Regression Model  $M$
  - 2: **Output:** Contact State  $s_t$
  - 3: **Step 1:** Noise Reduction
  - 4: Apply Kalman filter and smoothing:
  - 5:  $\hat{d}_t \leftarrow \text{Noise\_Reduction}(\hat{d}_t)$
  - 6: **Step 2:** Feature Extraction
  - 7: Current Value:  $V(t) \leftarrow \hat{d}_t$
  - 8: Local Average:  $A(t) \leftarrow \text{Moving\_Average}(\hat{d}_{t-w:t})$
  - 9: Local Trend:  $T(t) \leftarrow \text{Least\_Square}(\hat{d}_{t-w:t})$
  - 10: Cluster:  $C(t) \leftarrow \begin{cases} \text{No Contact} & \text{if } \hat{d}_t < a \\ \text{Light Contact} & \text{if } a \leq \hat{d}_t < b \\ \text{Forceful Contact} & \text{if } \hat{d}_t \geq b \end{cases}$
  - 11: Features:  $F(t) \leftarrow [V(t), A(t), T(t), C(t)]$
  - 12: **Step 3:** Contact Detection  $s_t \leftarrow M(F(t))$
- 

2) *Feature Extraction:* The feature extraction step identifies key characteristics that impact contact detection. We construct four features, including *Current Value*, *Clusters*, *Local Trend*, and *Local Average* to represent the magnitude, trend of value, and possible contact state. The most recent  $\hat{d}$  is collected as *Current Value* to represent the current degree of depression. Due to the non-linear relationship between the depressed and detected distance shown in Fig. 3, we classify the contact state into three clusters according to the current detected distance providing prior knowledge for more accurate contact detection. The cluster could be no contact, light contact, or forceful contact, and classified by  $a$  and  $b$ , which are calculated by the K-Means clustering method on a collected dataset. These classification parameters are then applied to real-time  $\hat{d}$  to separate them into three independent clusters as the *Cluster* feature. We also considered the tendency of the detected distance data during contact and extracted the *Local Trend* feature from  $\hat{d}$  by applying the least square method as follows.

$$T(t) = \frac{w \sum_{i=t-w+1}^t x_i \hat{d}_i - \sum_{i=t-w+1}^t x_i \sum_{i=t-w+1}^t \hat{d}_i}{w \sum_{i=t-w+1}^t (x_i^2) - (\sum_{i=t-w+1}^t x_i)^2}$$

where the  $x_i \in \mathbb{N}$  is the index of the detected distance data. The  $w$  is the window size and is set to 10 to capture the trend within 0.5s. To represent the approximate magnitude of local data points with minimal interference from outliers, we also calculate *Local Average* with the same window size as follows.

$$A(t) = \frac{1}{w} \sum_{i=t-w+1}^t \hat{d}_i$$

3) *Contact Detection:* A Contact Detection Model is deployed to interpret the extracted features for contact detection. As shown in Algorithm 2, the module was trained by feature vectors and corresponding contact state. The feature vectors are extracted from the training dataset  $D_{train}$  with random contact states, while the label is annotated manually based on the recorded force data.

---

**Algorithm 2** Contact Detection Model Training

- 1: **Input:** Training set  $D$ , Contact force  $C$
  - 2: **Output:** Logistic regression model  $M$
  - 3: **Step 1:** Feature Preparation
  - 4: Extract features from training set:
  - 5:  $F(D) \leftarrow [T(D), C(D), V(D), A(D)]$
  - 6: **Step 2:** Label Preparation
  - 7: Assign labels based on contact force:
  - 8: Contact state  $Y \leftarrow \begin{cases} \text{Contact,} & \text{if } C > 0, \\ \text{No Contact,} & \text{if } C = 0. \end{cases}$
  - 9: **Step 3:** Model Training
  - 10: Train logistic regression model:
  - 11:  $M \leftarrow \text{Logistic\_Regression}(F(D), Y)$
- 

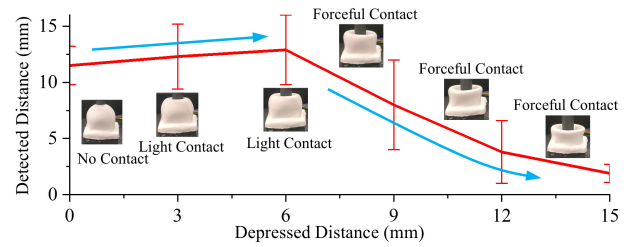


Fig. 5. The relationship between the mean detection detected and depressed distance. The error bars represent the standard deviation.

### III. RESULT & DISCUSSION

To validate the resolution, robustness, computational load, and accuracy of the sensor output, we conducted four experiments: (1) characterization of elastomer deformation detection and force resolution, (2) evaluation of the sensor's robustness under various interference conditions, (3) assessment of the sensor's output accuracy during multiple contact events, and (4) application of the sensor in real-world clothing contact detection scenarios with structurally or materially fluffy surfaces.

#### A. Detection of Elastomer Deformation & Force Resolution

We characterized the relationship between detected and depressed distance. The Fig. 5 shows the change in the detected distance along with the depressed distance. With the increase of depression, the detected distance rises from around 12 mm to around 13 mm and then down to around 4 mm, showing an overall nonlinearity. We then measured the MDCF (Minimum Detectable Contact Force) and softness of the contact sensor. The contact sensor was mounted on a vertically movable platform shown in Fig. 6(a), moving from the same height to lower levels at different speeds. During the motions, the sensor contacts a calibrated electronic balance (accuracy grade: OIML III, resolution: 0.001g, ZOG-TP203-500, GMM Technoworld Pte Ltd). The readings from the balance are converted to contact forces considering gravitational acceleration  $9.8066 \text{ m/s}^2$ . The contact force corresponding to the first detected contact data point is the MDCF. The results are illustrated in Fig. 6(b) revealing that the MDCF range of

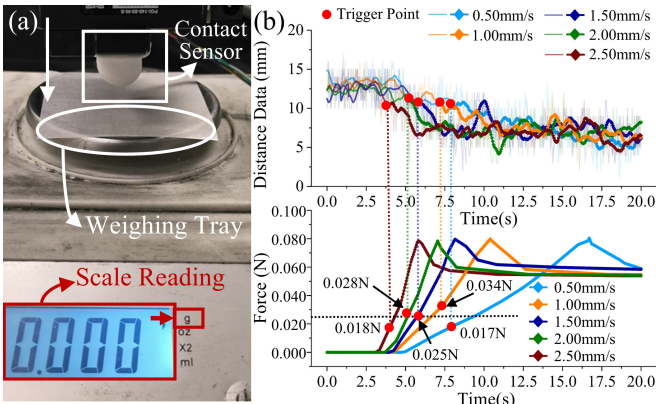


Fig. 6. Measurement of the MDCF at different speeds. (a) shows the setup of the measurement system. The upper part of (b) displays the raw and filtered distance data. The detected contact data points are marked, and the red marker indicates the first detected contact data point. The lower part of (b) presents the contact forces at different speeds.

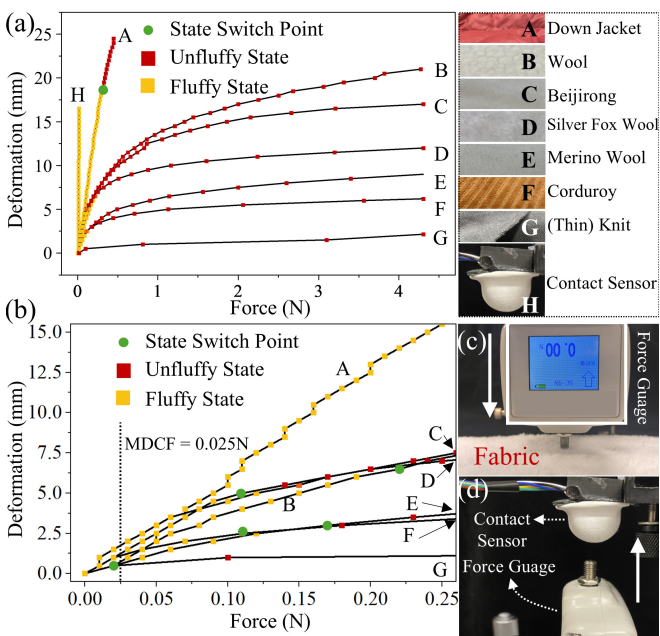


Fig. 7. Comparison of sensor and fabric softness. (a) shows the deformation of the sensor and fabric as the contact force increases. (b) is the partial enlargement of (a) showing the fluffiness state switch point of the fabric and the MDCF. (c) and (d) present the experimental setup for the testing of the softness of the fabric and sensor respectively. The white arrow indicates the motion direction of the force gauge.

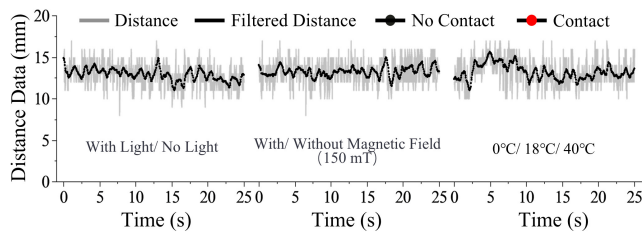


Fig. 8. The contact sensor data with no contact under varying light, magnetic field, and temperature.

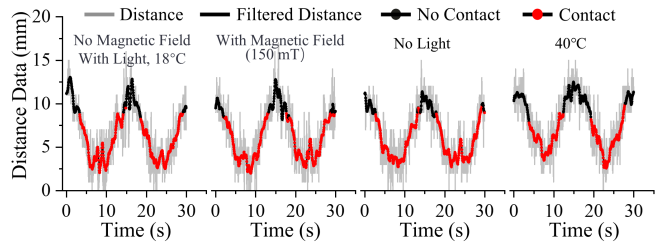


Fig. 9. The contact sensor data during fabric contact under varying light, magnetic field, and temperature.

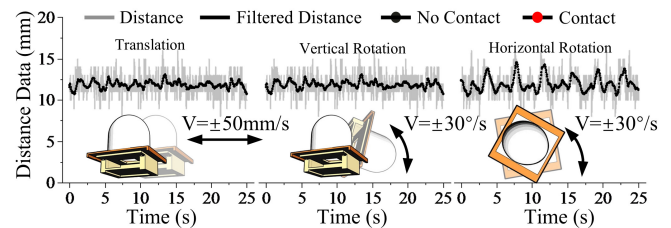


Fig. 10. The distance data and contact detection during movement.

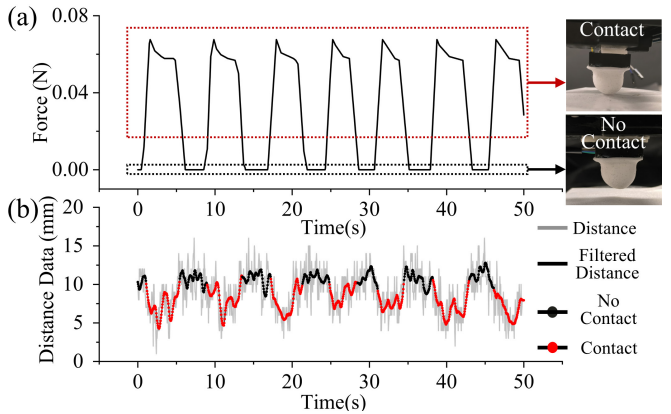


Fig. 11. The result of multiple contact detection. (a) shows the contact force indicating the contact states. (b) presents the distance data and contact detection results of the sensor.

the sensor is from 0.017 N to 0.034 N when the contact speed is between 0.5 and 2.5 mm/s.

To evaluate the softness of the sensor compared with that of the fabrics, we measured the force-distance curves. We deployed a force gauge (graduation: 0.01N, accuracy:  $\pm 0.01N$ , SC-5N, ShenCe, China) and a motion platform as shown in Fig. 7(c) and (d) to drive the sensor to contact the fabrics. The results, shown in Fig. 7(a) and (b), indicate that all fabrics deform with increasing contact force. The Down Jacket exhibits the fastest deformation, while the Knit fabric shows the slowest. The knitted fabric reaches an unfluffy state under minimal contact force, preventing the sensor from detecting contact in the fluffy state. Compared to other soft materials, the contact sensor demonstrates enough softness to detect contact in a fluffy state.

### B. Robustness under External Interference

To validate the robustness of the contact sensor against interference factors such as light, magnetic fields, and tem-

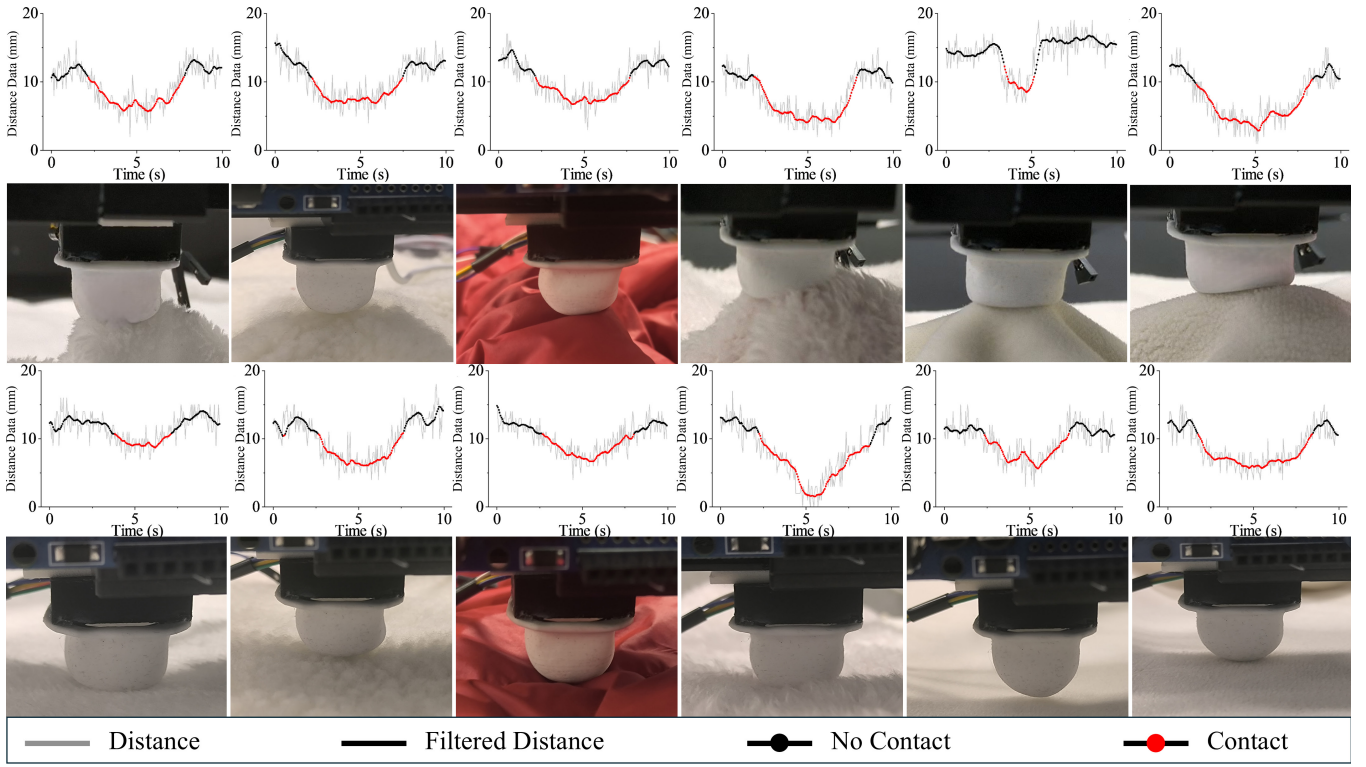


Fig. 12. Testing of contact sensors in real-world scenarios. The upper part of the figure shows contact with randomly placed fabric, while the lower portion depicts contact with flat-laid fabric. The detection results are provided, where the red segments indicate detected contacts.

perature, we placed the sensor in different conditions. We recorded the sensor's raw distance data, filtered data, and detection results, as presented in Fig. 8 and Fig. 9. The result shows that the contact sensor can work normally in environments with different interference.

To test the robustness of the sensor during movement, we tested the sensor with three types of motions: translation, vertical rotation, and horizontal rotation without contact. The translation speed is 50 mm/s, and the vertical and horizontal rotation speeds are 30°/s. The detected distance and the contact detection were recorded and are presented in Fig. 10. The result shows that the sensor correctly outputs "no contact" during movement (Fig. 9).

#### C. Real-time Capability & Detection Accuracy

To evaluate the contact detection accuracy of the sensor, we used a vertically movable platform to repeatedly engage the sensor with a balance. The balance reading was recorded, and we consider any external force applied as "contact". The force data and detection results are shown in Fig. 11. In 28 tries of contact, including 4000 contact detections, the accuracy of the contact detection achieves 95%. In each detection, the contact detection algorithm processed data within 7.5 ms with a CPU (Intel(R) Xeon(R) CPU, 2.20GHz).

#### D. Testing in Real-world Scenarios

To evaluate the contact sensor's detection performance in real-world applications, we conducted contact detection

tests on six different types of fabric that varied in softness. For each type, we performed two tests, one with random placement, which is primarily in structural fluffy state, and another with flat laying, which is primarily in material fluffy state. The contact sensor, driven by a motion platform, moves from high to low to make contact with the fabrics. The distance data and the detection results are presented in Fig. 12. The results indicate that the contact sensor successfully detects contact in the fluffy state across different fabric types and fluffiness levels.

#### IV. CONCLUSION

In this work, we present a contact sensor characterized by high force resolution, robust performance, real-time data processing, and high detection accuracy. The sensor detects contact by measuring elastomer deformation. We developed a casting-based fabrication method for the elastomer and analyzed contact conditions, categorizing three distinct contact states of the sensor and three fluffiness states of the fabric. Our contact detection algorithm comprises three steps: noise reduction, feature extraction, and contact detection. Experimental results demonstrate that the sensor can detect contact forces as low as 0.017 N and remains unaffected by environmental interference, such as light, magnetic fields, temperature variations, and motion. The algorithm achieves a short computation time of 7.5 ms and an accuracy of up to 95%. Finally, the sensor was evaluated in real-world fabric contact detection scenarios, confirming its practical applicability.

## REFERENCES

- [1] N. Yu, Z. Zhang, Q. Xu, E. Firdaus, and J. Lin, "An improved method for cloth pattern cutting based on Holistically-nested Edge Detection," in *2021 IEEE 10th Data Driven Control and Learning Systems Conference (DDCLS)*, May 2021, pp. 1246–1251.
- [2] K. Tang, F. Tokuda, A. Seino, A. Kobayashi, N. C. Tien, and K. Kosuge, "Time-Scaling Modeling and Control of Robotic Sewing System," *IEEE/ASME Transactions on Mechatronics*, vol. 29, no. 4, pp. 3166–3174, Aug. 2024.
- [3] Y. Li, X. Hu, D. Xu, Y. Yue, E. Grinspun, and P. K. Allen, "Multi-sensor surface analysis for robotic ironing," in *2016 IEEE International Conference on Robotics and Automation (ICRA)*, May 2016, pp. 5670–5676.
- [4] L. Yariv, Y. Kasten, D. Moran, M. Galun, M. Atzmon, B. Ronen, and Y. Lipman, "Multiview Neural Surface Reconstruction by Disentangling Geometry and Appearance," in *Advances in Neural Information Processing Systems*, vol. 33. Curran Associates, Inc., 2020, pp. 2492–2502.
- [5] I. Vizzo, X. Chen, N. Chebrolu, J. Behley, and C. Stachniss, "Poisson Surface Reconstruction for LiDAR Odometry and Mapping," in *2021 IEEE International Conference on Robotics and Automation (ICRA)*, May 2021, pp. 5624–5630.
- [6] A. M. L. Kappers, "Human perception of shape from touch," *Philosophical Transactions of the Royal Society B: Biological Sciences*, vol. 366, no. 1581, pp. 3106–3114, Nov. 2011.
- [7] R. L. Klatzky and S. J. Lederman, "Haptic object perception: Spatial dimensionality and relation to vision," *Philosophical Transactions of the Royal Society B: Biological Sciences*, vol. 366, no. 1581, pp. 3097–3105, Nov. 2011.
- [8] C. M. Boutry, M. Negre, M. Jorda, O. Vardoulis, A. Chortos, O. Khatib, and Z. Bao, "A hierarchically patterned, bioinspired e-skin able to detect the direction of applied pressure for robotics," *Science Robotics*, vol. 3, no. 24, p. eaau6914, Nov. 2018.
- [9] N. F. Lepora, U. Martinez-Hernandez, M. Evans, L. Natale, G. Metta, and T. J. Prescott, "Tactile Superresolution and Biomimetic Hyperacuity," *IEEE Transactions on Robotics*, vol. 31, no. 3, pp. 605–618, Jun. 2015.
- [10] J. Park, M. Kim, Y. Lee, H. S. Lee, and H. Ko, "Fingertip skin-inspired microstructured ferroelectric skins discriminate static/dynamic pressure and temperature stimuli," *Science Advances*, vol. 1, no. 9, p. e1500661, Oct. 2015.
- [11] Y. Wei and Q. Xu, "An overview of micro-force sensing techniques," *Sensors and Actuators A: Physical*, vol. 234, pp. 359–374, Oct. 2015.
- [12] D. Li, X. Li, H. Zhao, D. Ge, and H. Ding, "Robotic Multiple Peg-in-Hole Assembly with Deviation Estimation and Fast Insertion Control," *IEEE Transactions on Industrial Electronics*, pp. 1–11, 2024.
- [13] M. A. Lee, Y. Zhu, P. Zachares, M. Tan, K. Srinivasan, S. Savarese, L. Fei-Fei, A. Garg, and J. Bohg, "Making Sense of Vision and Touch: Learning Multimodal Representations for Contact-Rich Tasks," *IEEE Transactions on Robotics*, vol. 36, no. 3, pp. 582–596, Jun. 2020.
- [14] U. Kim, D.-H. Lee, Y. B. Kim, D.-Y. Seok, and H. R. Choi, "A Novel Six-Axis Force/Torque Sensor for Robotic Applications," *IEEE/ASME Transactions on Mechatronics*, vol. 22, no. 3, pp. 1381–1391, Jun. 2017.
- [15] I. H. Taylor, S. Dong, and A. Rodriguez, "GelSlim 3.0: High-Resolution Measurement of Shape, Force and Slip in a Compact Tactile-Sensing Finger," in *2022 International Conference on Robotics and Automation (ICRA)*, May 2022, pp. 10 781–10 787.
- [16] A. Padmanabha, F. Ebert, S. Tian, R. Calandra, C. Finn, and S. Levine, "OmniTact: A Multi-Directional High-Resolution Touch Sensor," in *2020 IEEE International Conference on Robotics and Automation (ICRA)*, May 2020, pp. 618–624.
- [17] W. Xu, G. Zhou, Y. Zhou, Z. Zou, J. Wang, W. Wu, and X. Li, "A Vision-Based Tactile Sensing System for Multimodal Contact Information Perception via Neural Network," *IEEE Transactions on Instrumentation and Measurement*, vol. 73, pp. 1–11, 2024.
- [18] Y. Yan, Z. Hu, Z. Yang, W. Yuan, C. Song, J. Pan, and Y. Shen, "Soft magnetic skin for super-resolution tactile sensing with force self-decoupling," *Science Robotics*, vol. 6, no. 51, p. eabc8801, Feb. 2021.
- [19] R. S. Dahiya, G. Metta, M. Valle, and G. Sandini, "Tactile Sensing—From Humans to Humanoids," *IEEE Transactions on Robotics*, vol. 26, no. 1, pp. 1–20, Feb. 2010.
- [20] P. Piacenza, S. Sherman, and M. Ciocarlie, "Data-Driven Super-Resolution on a Tactile Dome," *IEEE Robotics and Automation Letters*, vol. 3, no. 3, pp. 1434–1441, Jul. 2018.
- [21] G. De Maria, C. Natale, and S. Pirozzi, "Force/tactile sensor for robotic applications," *Sensors and Actuators A: Physical*, vol. 175, pp. 60–72, Mar. 2012.